# Seed-Induced Pathway Control of Low-Dispersity Polymorphic Microcrystals of pi-Conjugated Molecules

*Yulian Li,* [†#] *Xiaohui Lan,* [‡#] *Zuofang Feng,* [†] *Lulu Zhang,* [†] *Wai-Yeung Wong,* [§*] *Zhengong Meng,* [‡*] *and Yilong Lei*[†*]

[†]Department of Chemistry, School of Science, Tianjin University, Tianjin 300072, P. R. China.

[‡]School of Flexible Electronics (Future Technologies) & Institute of Advanced Materials, Nanjing Tech University, Nanjing 211800, P. R. China

[§]Department of Applied Biology and Chemical Technology and Research Institute for Smart Energy, The Hong Kong Polytechnic University, Hung Hom, Hong Kong, P. R. China

**ABSTRACT:** The precise synthesis of polymorphic π-conjugated micro- and nanocrystals remains challenging due to the existence of competing assembled pathways. Here we realize controlled polymorphic microcrystals of a dicyanodistyrylbenzene derivative (**A**) via seed-induced pathway transformation. Small-sized α-**A** nanocrystals that are thermodynamically stable are preformed via a microspacing physical vapor transport (PVT) method. These vapor-grown nanocrystals function as seeds and tailor the assembled pathway of potentially occurring β-**A** microcrystals corresponding to kinetically metastable products, leading to the controlled growth

of α-**A** microcrystals. Intriguingly, the length and surface area of the seed-induced α-**A** microcrystals increase linearly with the molar ratios of added monomer to seeds. Such a seed-induced transformation strategy resembles living supramolecular polymerization of amphiphilic dyes, which is also applicable to more polymorphic π-conjugated microcrystals even binary alloys. This work provides deeper insights in controlling assembled pathways and polymorphs of π-conjugated systems and producing organic microcrystals of narrow size distributions.

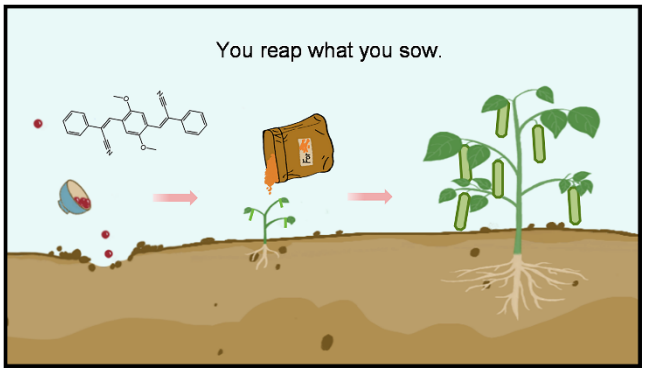


The development of living polymerization has allowed a good access to covalent polymers with narrow molecular weight distributions.[1,2] Following the similar living growth concept, a method termed living crystallization-driven self-assembly (CDSA) has demonstrated its great efficacy in synthesizing low-dispersity micellar nanoparticles of block copolymers (BCPs).[3–11] The most popular BCPs referring to living CDSA (Figure 1a) generally contain a crystallizable polyferrocenyldimethylsilane (PFS) core-forming block,[3–7] which are apt to crystallize in polydisperse 1D and 2D micelles. Using these fragmented micelles induced by ultrasonication as seeds, elongated 1D and 2D nanoparticles with narrow size distributions are obtained by addition of the identical or different PFS-containing BCP unimers. Such a living growth behavior (also defined as living supramolecular polymerization,[12–17] has been elaborately extended to

amphiphilic π-stacked dyes, such as zinc porphyrins[18,19] and perylene bisimides amphiphiles.[20–22] Using this method, kinetically trapped species transforms into the thermodynamically favored aggregates in a short time upon addition of the fragmented seeds of the latter (Figure 1b).[12,13,18–22] Consequently, elongated and multiblock supramolecular polymeric nanoparticles with controlled lengths and/or area are achieved by varying the ratios of the metastable aggregates to the seeds.

Noteworthy is that the elaborate control of pathway complexity for amphiphilic π-stacked dyes is the key to realizing supramolecular polymorphism and further living supramolecular polymerization in which the packing arrangements of different polymorphs are governed by π−π stacking and/or hydrogen-bonding patterns.[23–26] The resulting thermodynamical and kinetical aggregates in supramolecular systems resemble their polymorphic counterparts obtained from nonamphiphilic molecular crystals without the modification of long alkoxyl groups or large π-conjugated sidegroups. Impressively, π-conjugated small molecules that have been widely used to fabricate high-efficiency optoelectronic devices and usually crystallize in two or more polymorphs.[27–42] Depending on proper processing conditions, such as concentration and temperature variations, kinetically metastable (β-form) and thermodynamically favored (α-form) organic microcrystals are both realized,[43,44] which endow them with largely different optoelectronic performances. Given small sizes of supramolecular aggregates of an amphiphilic dye, it is difficult to distinguish and characterize the assemblies and various techniques involving spectroscopic tools and atomic force microscope are used to recognize the products. On the contrary, polymorphic π-conjugated micro- and nanocrystals can be easily identified by their disparate shapes, emission colors, and stabilities. To date, the research on polymorphic molecular crystals has achieved great successes, however, pathway control over low-dispersity crystals of a certain polymorph remains challenging due to the deficiency in understanding pathway complexity

in crystalline molecular assemblies. It can be anticipated that precise size control of molecular crystals shows a great significance for practical applications due to the excellent consistency of optoelectronic performances.

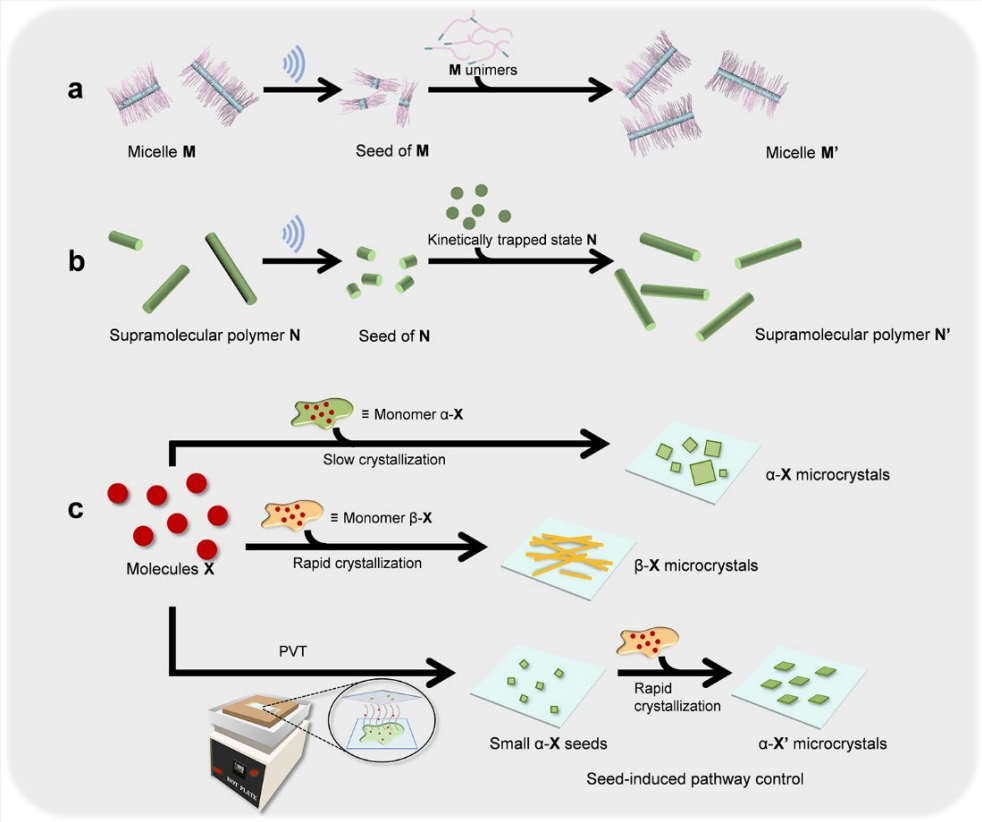


**Figure 1.** (a, b) Schematic illustration of (a) the living CDSA and (b) living supramolecular polymerization processes to synthesize low-dispersity nanoparticles of amphiphilic BCPs and π-stacked dyes, respectively. (c) Schematic showing a seed-induced strategy for pathway control of polymorphic microcrystals of π-conjugated small molecules used in the present work in which small-sized α-**X** micro- and nanocrystals obtained via a vapor-phase PVT route are used as seeds to allow further growth of the monomer suitable for kinetically metastable β-**X** microcrystals.

Herein, we initially realized thermodynamically stable α-form microribbons (MRs) and kinetically metastable β-form microwires (MWs) of a π-conjugated dicyanodistyrylbenzene-

derived compound (**A**, Figure 2a) by controlling the pathway complexity. Small-sized α-**A** nanoribbons (NRs) obtained via a convenient vapor-phase route acted as seeds to modulate the assembled pathway of potentially occurring β-**A** MWs. Consequently, elongated α-**A** MRs with high crystallinity and narrow size distributions were readily obtained. On the contrary, polymorph transformation cannot occur upon employing the vapor-grown β-**A** assemblies as seeds. Apart from 1D microcrystals of **A**, other polymorphic π-conjugated compounds that can crystallize in 2D sheet-like morphologies also undergo pathway transformation in the presence of seeds to yield uniform α-form microsheets in similar living manners.

As a variant of the living CDSA seeded growth approach, thermal or solvent-induced self-seeding method[45–47] has demonstrated the efficacy in synthesizing low-dispersity micelles of homopolymers and BCPs in which the surviving micelle fragments obtained by heating or addition of a good solvent function as seeds to induce monomer growth. To enable the controlled growth of polymorphic π-conjugated microcrystals, we rationally devised a two-step synthetic route which involves vapor-phase seed preparation (thermodynamically stable polymorph) and the subsequent solution-phase seed-induced pathway control (Figure 1c).

As documented previously,[43,44] several nonamphiphilic π-conjugated molecules yield different polymorphs by tailoring their crystallization rates, such as fast and slow cooling. The competing assembled pathways make it possible to realize the controlled growth of organic microcrystals by addition of seed crystals. Excitingly, a recently-developed vapor-phase assembly route called microspacing physical vapor transport (PVT)[48,49] can produce well-dispersed small-sized MWs and the MW tips at high temperature remain active to further epitaxial growth.[50] We conjectured that, upon utilizing the vapor-grown α-form assemblies of a π-conjugated compound as seeds,

controlled pathways may be realized by inhibiting potentially occurring β-form products and thus forming α-form species exclusively.

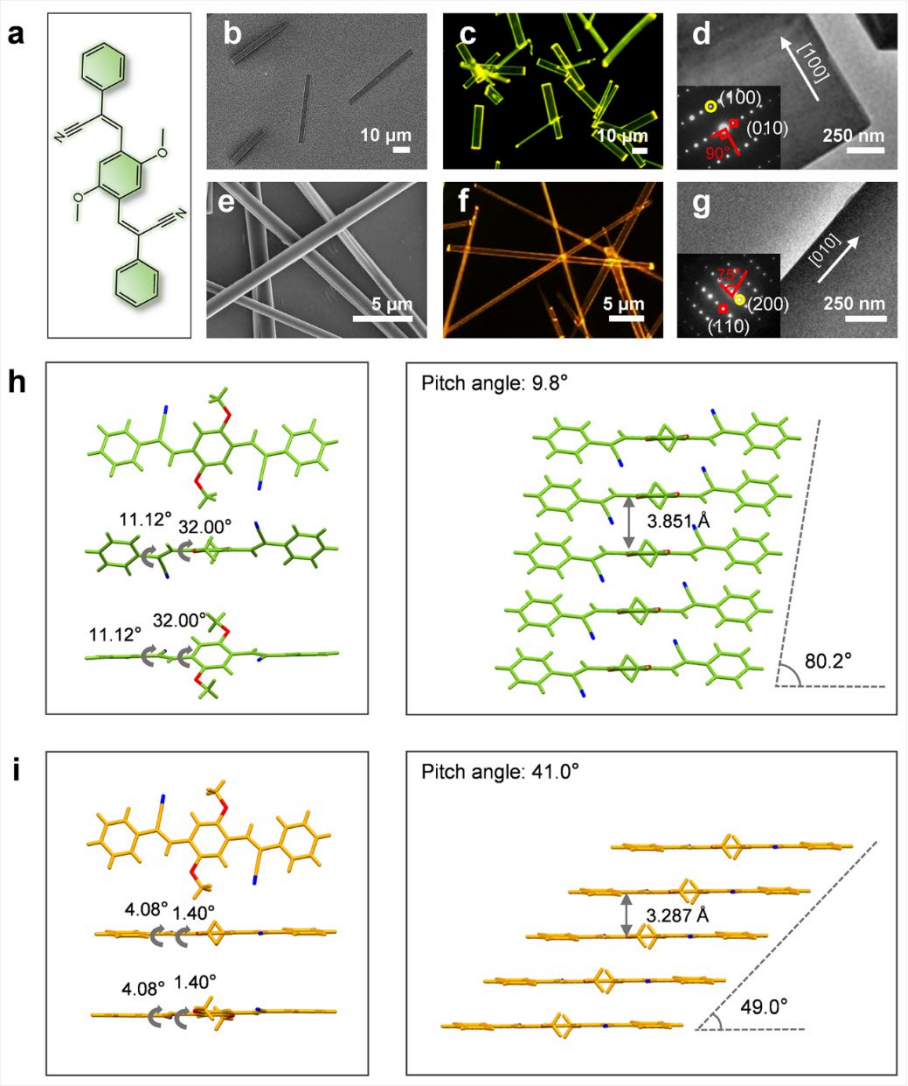


**Figure 2.** (a) Chemical structure of **A**. (b, e) SEM and (c, f) FM images of (b, c) α- and (e, f) β-**A** microcrystals as well as the corresponding (d, g) TEM images. Insets shown in d, g represent SAED patterns of single typical α-**A** MR and β-**A** MW. All samples were excited by UV light. (h, i) Molecular geometries and packing modes in the single crystals of (h) α- and (i) β-**A** as well as counter pitch angles.

As a conceptual validation, we specifically designed and synthesized a π-conjugated molecule **A** by Knoevenagel condensation reaction considering the high fluorescence efficiencies of DSB derivatives.[51–53] We first examined the thermodynamic and kinetic products by modulation of pathway complexity of **A**. Upon slow evaporation of **A** solution from THF/1,4-dioxane/cyclohexane (v/v/v = 3:2:5, $C_{\mathbf{A}}$ = 9 mM), 1D rectangular MRs with well-defined appearances were obtained, as revealed by SEM observation (Figure 2b). Under UV light excitation, fluorescence microscope result (FM, Figure 2c) reveals that these MRs show bright yellow-green emissions at their edges and tips. Fast crystallization of **A** solution from THF/1,4-dioxane/ethanol (v/v/v = 3:2:15, $C_{\mathbf{A}}$ = 4.5 mM) gave 1D MWs (Figure 2e,f), which display orange emissions. The relatively weaker emissions from the main parts of 1D microcrystals indicate optical waveguide behaviors, resulting from high crystallinity and well-defined appearance.[54] We identified 1D MRs and MWs as α- and β-**A** products, respectively, depending on their crystallization rates.

To exactly identify the crystal structures of **A** MRs and MWs, large-sized crystals suitable for single-crystal X-ray diffraction (SCXRD) analysis were slowly grown from THF/1,4-dioxane and THF/1,4-dioxane/ethanol, respectively. As expected, the crystallographic data (Table S1) verifies that **A** formed two different crystal phases, which match with powder X-ray diffraction (PXRD) patterns of **A** MRs and MWs (Figure S1). Additionally, thermodynamically stable α-**A** MRs and kinetically metastable β-**A** MWs were both obtained by controlling assembled pathways. Combined with the predicted morphologies, typical crystal facets of these two polymorphic microcrystals were identified (Figure S2). Their 1D growth behaviors can be attributed to π–π stacking in α- and β-**A**. TEM images of single typical MR and MW of **A** and corresponding selected-area electron diffraction (SAED) patterns reveal their single crystal structures, as further

revealed by the birefringence information collected by polarized optical microscopy (POM, Figure S3). Moreover, α-**A** MR and β-**A** MW preferentially grow along the [100] and [010] directions (Figure 2d and g), respectively

We further performed time-dependent FM and PXRD measurements by heating β-**A** MWs at 140 ℃ (Figures S4 and S5). Upon prolonging the heating time, the orange emissions gradually convert into yellow-green light and the transformation complete basically at $t$ = 60 min. Meanwhile, PXRD data shows that the peaks derived from α-**A** become stronger, while those from β-**A** crystals completely disappear over 1 h, undoubtedly verifying polymorph transformation from β-**A** to α-**A**. The distinct differences between MRs and MWs of **A** in shapes, emission colors, and stabilities reveal the competing assembled pathways.[55,56] For convenience, the monomer solution of β-**A** MWs was denoted as $\mathbf{M_{\beta\text{-}A}}$.

Notably, α- and β-**A** adopt distinct molecular geometries and packing patterns (Figure 2h,i). The long molecular axes in α-**A** are noticeably tilted (torsion angles: 11.12° and 32.0°) and small interlayer slips of adjacent molecules lead to a counter pitch angle of 80.2° and an interplane distance of 3.851 Å. While the long axes in β-**A** are nearly planarized (torsion angles: 4.08° and 1.40°) and the alternating donor-acceptor (D-A) structures consisting of electron-rich alkoxy-substituted phenyl rings and electron-deficient cyano-vinylene units enable the D and A segments of neighboring molecules to stack on top of each other, this gives a small pitch angle of 41.0° and an interplane distance of 3.287 Å. Apparently, **A** molecules in α- and β-**A** adopt parallel and slipped stacking, respectively, that are contrary to DSB derivatives bearing two terminal amides.[51] Benefiting from intermolecular π–π stacking, α-**A** MRs and β-**A** MWs both show red-shifted emissions relative to the monomer solution (Figure S6). While slipped stacking rather than dimerization caused by intermolecular charge transfer (CT) interactions leads to longer-

wavelength emission of β-**A** MWs. Photoluminescence (PL) spectra reveal that α-**A** MRs exhibit a PL band centered at 552 nm with a quantum yield of 95.1%, while β-**A** MWs display a broader PL band at 570 nm with a quantum yield of 82% (Table S2). Notably, fluorescence decay measurements (Figure S7) reveal that PL lifetime of β-**A** MWs is significantly greater than that of α-**A** MRs ($\tau_{\beta\text{-}\mathbf{A}}$ = 25.08 ns; $\tau_{\alpha\text{-}\mathbf{A}}$ = 9.89 ns, Table S3), further clarifying intermolecular CT interactions in β-**A**.

In general, fragmented nanoparticles of amphiphilic BCPs and dyes obtained by ultrasonication serve as living seeds and more applicable synthetic approaches remain elusive. Considering the living growth behaviors of 1D MWs of nonamphiphilic π-conjugated molecules (e.g., 9,10-dicyanoanthracene, abbreviated as DCA) formed via a microspacing PVT technique (Figure 3a),[50] we applied this vapor-phase route to synthesize **A** seed crystals without using an inert gas. Specifically, a glass coverslip spin-coated by a THF solution of **A** ($C_{\mathbf{A}}$ = 0.13 mM, V = 6 μL, denoted as $\mathbf{M}_{\mathbf{seed}}$) was used as a bottom substrate and another coverslip as a top substrate, separated by multilayer coverslips. The hot plate was heated to 180 ℃ for 8 min, and **A** vapor generated by sublimation underwent short-distance transport ($H$ = 600 μm) and crystallized on the top substrate due to the temperature differences between the top and bottom substrates.

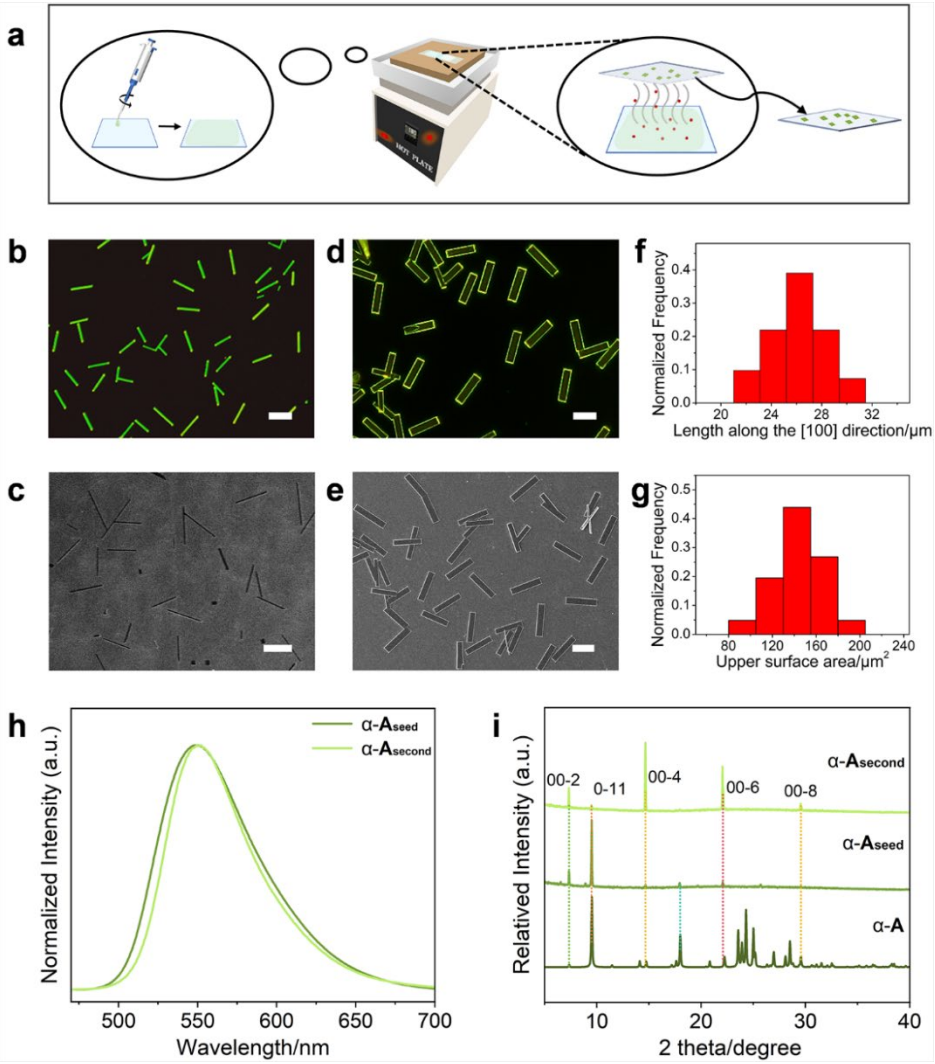


**Figure 3.** (a) Schematic showing a microspacing PVT technique for the preparation of small-sized organic crystals. (b, d) FM and (c, e) SEM images of (b, c) small-sized **A** crystals obtained through a PVT technique and (d, e) the assembled products obtained by addition of the monomer solution of β-**A** MWs on the preformed α-**A** assemblies. (f) Contour length and (g) area distributions of the resultant **A** MRs via seeded growth. All samples were excited by UV light. Scale bar, 20 μm. (h, i) PL spectra and PXRD patterns of vapor-grown **A** NRs (α-$\mathbf{A}_{\mathbf{seed}}$) and seed-induced **A** MRs (α-$\mathbf{A}_{\mathbf{second}}$). The excitation wavelength was 450 nm. For comparison, SCXRD pattern of α-**A** is also indicated.

Such a convenient PVT technique gave small-sized assemblies by maintaining **A** solution at low concentration (Figure 3b and c). These thin 1D crystals also emit yellow-green fluorescence under UV excitation and they have a length of about 21.7 μm. Atomic force microscope (AFM) observation reveals that **A** assemblies have a width of around 1.1 μm and a height of 174 nm (Figure S8a and b). PXRD pattern and PL spectrum of the vapor-grown **A** NRs coincide with those of α-**A** MRs (Figures 3h,i, S1, and S6), verifying that they share identical crystal form and emission color. Upon replacing THF with THF/1,4-dioxane/cyclohexane mixture (3:2:5), the microspacing PVT technique gave similar but unevenly dispersed α-**A** products (Figure S9) due to weak wetting behavior of the latter on the bottom substrate. Apparently, the crystal morphology and quality are closely related to the temperature of the hot plate and the distance (*H*) between the bottom and top substrates (Figure S10). Note that the living character of the vapor-grown DCA MWs depended on the temperature and the MWs were deactivated upon cooling to room temperature.[50] However, we anticipated that, upon partial dissolution, these vapor-grown **A** NRs would be capable of being activated and initiating further monomer growth by analogy with a solvent-induced self-seeding protocol.[45–47]

Based on the above analysis and assumptions, we preliminarily exemplified the possibility of seed-induced pathway control by addition of a 20 μL of $\mathbf{M}_{\beta\text{-}\mathbf{A}}$ solution onto the vapor-grown α-**A** NRs. After rapid evaporation of the solution, pure high-quality yellow-green-emitting MRs instead of orange-emitting MWs were obtained (Figure 3d,e), accompanied by noticeable size increase in comparison with the preformed α-**A** NRs. Based on the contour length and area distributions (Figure 3f,g), it can be estimated that newly-formed **A** MRs (denoted as $\alpha\text{-}\mathbf{A}_{\mathbf{second}}$) have a number-average length of 26.3 μm ($L_n$) and an area of 144 $\mu m^2$ ($A_n$), which correspond to low dispersities ($L_w/L_n$ = 1.011 and $A_w/A_n$ = 1.026, in which $L_w$ and $A_w$ are the weight-average length and area,

respectively). AFM result unveils that they have a uniform height of 783 nm (Figure S8c,d). Besides the identical emission color (Figure 3h), PXRD pattern of α-$\mathbf{A}_{\mathbf{second}}$ MRs reveals that they share the same crystal phase with the initial α-**A** NRs or MRs (Figure 3i). The existence of α-**A** NRs inhibits the assembly of $\mathbf{M}_{\mathbf{\beta\text{-}A}}$ and enables the transformation into α-**A** MRs that resembles seed-induced supramolecular polymerization of an amphiphilic dye, undoubtedly verifying that small-sized α-**A** nanocrystals function as seeds (α-$\mathbf{A}_{\mathbf{seed}}$) to favor further homoepitaxial growth.

For comparison, we reversed the experimental conditions by using vapor-grown β-**A** assemblies as seeds (β-$\mathbf{A}_{\mathbf{seed}}$) and adding a precursor solution of α-**A** MRs as a monomer ($\mathbf{M}_{\mathbf{\alpha\text{-}A}}$). Using the microspacing PVT technique, wire- or ribbon-like β-**A** micro- and nanocrystals with orange emission were synthesized, as verified by PL spectrum and PXRD pattern (Figure S11a,b,e,f). Upon addition of a $\mathbf{M}_{\mathbf{\alpha\text{-}A}}$ solution, the prefabricated β-**A** crystals converted into high-dispersity green-emitting MRs or MWs (Figure S11c,d), which matched well with α-**A**. We inferred that the β-**A** assemblies may undergo complete dissolution in the unsaturated $\mathbf{M}_{\mathbf{\alpha\text{-}A}}$ solution and recrystallization led to α-**A** MRs and MWs. Accordingly, $\mathbf{M}_{\mathbf{\alpha\text{-}A}}$ cannot assemble into kinetically metastable β-**A** MRs by utilizing a seeding strategy.

The ability of the seed-induced pathway transformation approach was deeply revealed by varying the monomer to seed molar ratios ($n$/$n$), as shown in Figure 4. To ensure that the numbers of α-**A** seed nanocrystals were constant, the concentrations and amounts of precursor solutions of **A** remained the same ($C_A$' = 0.05 mM, V = 1 μL, denoted as $\mathbf{M}_{\mathbf{seed}}$'). These new seeds (α-$\mathbf{A}_{\mathbf{seed}}$') formed by microspacing PVT have smaller dimensions (ca. 13.4 μm × 806 nm × 73 nm, Figures 4a and S12) than the seeds obtained from $\mathbf{M}_{\mathbf{seed}}$. After addition of different amounts of $\mathbf{M}_{\mathbf{\beta\text{-}A}}$ solutions (V = 3, 5, 7, 9, 13 μL), low-dispersity yellow-green-emitting MRs were still obtained, accompanied by increased sizes. By further checking the SEM results (Figure 4b), one can see that

these α-**A** MRs (denoted as α-$\mathbf{A}_{\mathbf{second}}$') keep smooth surfaces and well-defined shapes. POM images of α-$\mathbf{A}_{\mathbf{second}}$' MRs clearly validate their high-quality crystallinity (Figure S13). Apparently, $\mathbf{M}_{\mathbf{\beta\text{-}A}}$ can exclusively assemble into α-**A** MRs rather than β-**A** MWs in the presence of vapor-grown α-$\mathbf{A}_{\mathbf{seed}}$' nanocrystals.

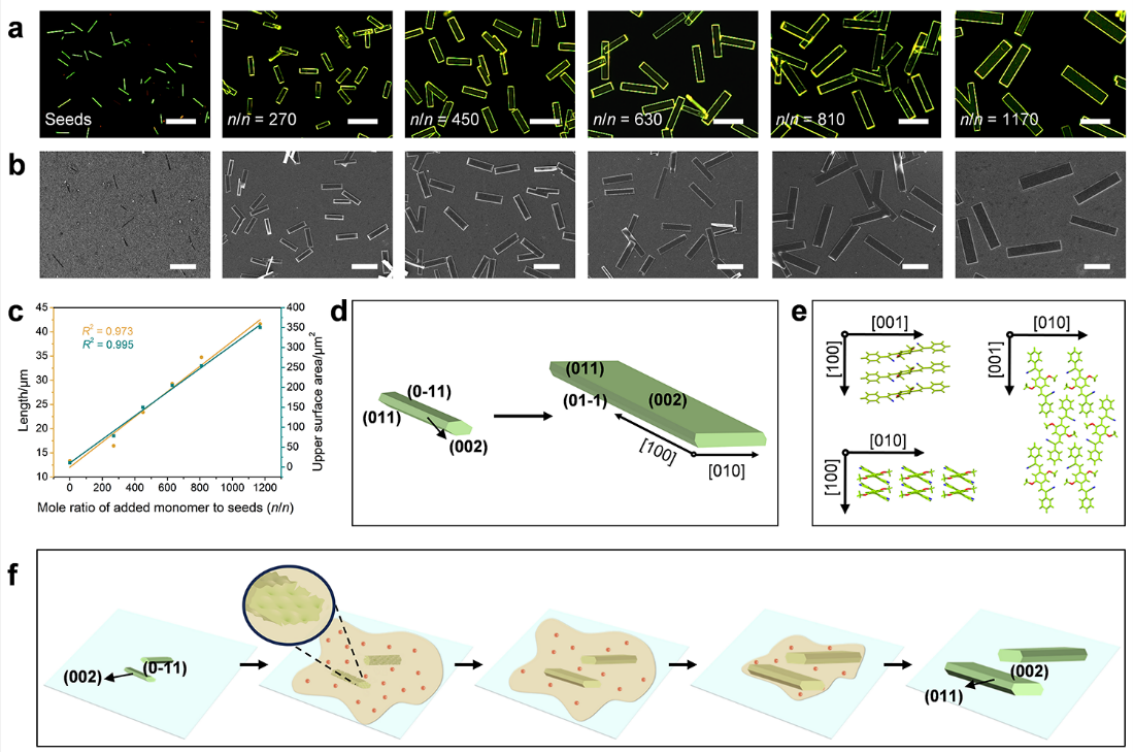


**Figure 4.** (a) FM and b) SEM images of α-$\mathbf{A}_{\mathbf{seed}}$′ NRs and α-$\mathbf{A}_{\mathbf{second}}$′ MRs formed at variable monomer to seed molar ratios (*n*/*n*). All samples were excited by UV light. Scale bar, 20 μm. (c) Plots and fitted curves of the length and surface area of α-$\mathbf{A}_{\mathbf{second}}$′ MRs versus variable *n*/*n*. (d) Schematic showing individual α-$\mathbf{A}_{\mathbf{seed}}$′ NR and α-$\mathbf{A}_{\mathbf{second}}$′ MR with specific crystal facets and e) the corresponding molecular packing viewed down the *b*, *c*, and *a* axes. (f) Schematic illustration of the processes of seed-induced pathway transformation for low-dispersity α-**A** MRs.

AFM images shown in Figure S14 further reveal that α-$\mathbf{A}_{\mathbf{second}}$' MRs possess small surface roughness and α-$\mathbf{A}_{\mathbf{seed}}$' nanocrystals undergo significant increases in length and width after addition

of **M**$_{\beta\text{-}\mathbf{A}}$. The number-average length $L_n$ of α-**A**$_{\mathbf{second}}$' MRs varies from 16.5 μm at $n/n$ = 270 to 41.6 μm at $n/n$ = 1170, while the average area $A_n$ increases from 79 μm$^2$ to 350 μm$^2$. Similar to the assembled products formed by living CDSA or living supramolecular polymerization,[3–22] α-**A**$_{\mathbf{second}}$' MRs also have narrow length and area dispersities ($L_w/L_n$ = 1.015 and $A_w/A_n$ = 1.051 for $n/n$ = 270, Table S4). The length and surface area of α-**A**$_{\mathbf{second}}$' MRs were found to be linearly proportional to $n/n$ (Figure 4c). This implies that the seed-induced pathway transformation approach allows a good access to low-dispersity **A** MRs with controlled areas, which is analogue to 2D living growth of polymer micelles.[8,13]

Tracing back to AFM observations (Figures S8a,b and S12), we noticed that the vapor-phase route gave α-**A**$_{\mathbf{seed}}$/**A**$_{\mathbf{seed}}$' NRs with hexagonal cross-sections, as further verified by high-magnification SEM images (Figure S15). Combined with PXRD pattern of α-**A**$_{\mathbf{seed}}$ NRs and simulated growth morphology of α-**A**, it can be verified that the top and bottom surfaces of these seed NRs are enclosed by the equivalent (0-11) and (01-1) planes. Moreover, only a small portion of (002) side plane was identified by XRD analysis owing to thin thickness of the seeds. After seeded growth, the (002) plane turns into the dominated top plane and the (0-11) plane is nearly invisible (Figure 4d). Apparently, α-**A**$_{\mathbf{seed}}$/**A**$_{\mathbf{seed}}$' NRs underwent huge width increases but minor height changes (Figure S16). For example, α-**A**$_{\mathbf{second}}$' MRs have a uniform width of 4.7 μm and a height of 564 nm at $n/n$ = 270. It appears obvious that the seed NRs elongate mainly along the [010] and [100] directions after addition of **M**$_{\beta\text{-}\mathbf{A}}$ solutions. However, it remains unclear what causes such an unconventional living seeded growth.

To uncover the cause, we specifically examined molecular packing and interaction types of α-**A** viewed down the $a$, $b$, and $c$ axes (Figure 4e). Notably, the adjacent **A** molecules along the [100] direction are connected via π–π stacking, while those along the [010] direction are linked via C–

H···N and C–H···π interactions. It seems reasonable that strong intermolecular interactions on the (100) and (010) planes allow an access to preferential growth of the newly added **A** molecules. Contrarily, the exposed phenyl groups of **A** molecules on the (001) plane would play an opposite role, thus suppressing the height increase. Moreover, for α-**A**, the calculated attachment energies from the (100), (010), and (001) planes (Table S5) follow an order of $E_{att}(100) < E_{att}(010) < E_{att}(002)$, revealing faster growth of α-$\mathbf{A}_{\mathbf{seed}}$' NRs on the (100) plane than the (010) plane.

The detailed processes and mechanism of seed-induced pathway transformation were also proposed (Figure 4f). We inferred that the addition of $\mathbf{M}_{\mathbf{\beta\text{-}A}}$ led to faster dissolution of α-**A** seed NRs on the (100) and (011) planes than the (002) plane due to more loose molecular packing of the former. While highly saturated $\mathbf{M}_{\mathbf{\beta\text{-}A}}$ solution facilitates partial dissolution of the seed NRs that enables the reactivation of these planes. As the mixture solvents (THF/1,4-dioxane/ethanol) evaporated, the solubility of **A** monomer molecules rapidly decreased, thus generating a higher degree of supersaturation. Free **A** molecules preferentially deposited on the active planes of the surviving NRs via a self-seeding protocol and evolved into MRs. The 1D growth habit of α-**A** also favors the elongation of **A** NRs along the [100] direction. The presence of α-**A** seed NRs suppressed self-nucleation of $\mathbf{M}_{\mathbf{\beta\text{-}A}}$ and the energy barriers between $\mathbf{M}_{\mathbf{\beta\text{-}A}}$ and α-**A** were almost completely eliminated, facilitating the conversion into α-**A** products. On the contrary, the energetically unfavorable transformation from $\mathbf{M}_{\mathbf{\alpha\text{-}A}}$ to β-**A** would not allow the vapor-grown β-**A** assemblies to act as seeds.

Considering their wide diversity and various assembled architectures, we expect to realize pathway control over more polymorphic organic microcrystals via such a seed-induced strategy. As representative cases, linear- and disc-shaped π-conjugated species (Figure 5), such as 2,7-diphenyl-9*H*-fluoren-9-one (**B**) and perylene (**C**), are also capable of forming α- and β-form

microcrystals.[43,44,57–59] Impressively, contrary to 1D wire-like **A** microcrystals, both **B** and **C** can crystallize in sheet-like morphologies, which initiate the possibility of creating uniform 2D microcrystals. Likewise, it still remains challenging to obtain high-purity polymorphic **B** and **C** crystals, let alone low-dispersity microcrystals. Fortunately, we obtained pure α- and β-form assemblies of **B** and **C** under optimal solution-phase conditions (Figures 5a,b,g,h and S17). For instance, **B** underwent competing assembled pathways to yield green-emitting α-form microsheets (MSs) and yellow-green-emitting β-form MWs, respectively, while α- and β-**C** were capable of generating yellow- and green-emitting MSs, respectively. PL spectra and PXRD patterns (Figures S18, S19, and Table S6) can be used to differentiate these thermodynamic and kinetic products. TEM images of single microcrystals and the corresponding SAED patterns (Figure S20) reveal their single crystalline natures, as further confirmed by POM results (Figure S21). We thereby inferred that α-**B** MS and β-**B** MW were preferentially grown along the [001] and [100] directions, respectively.

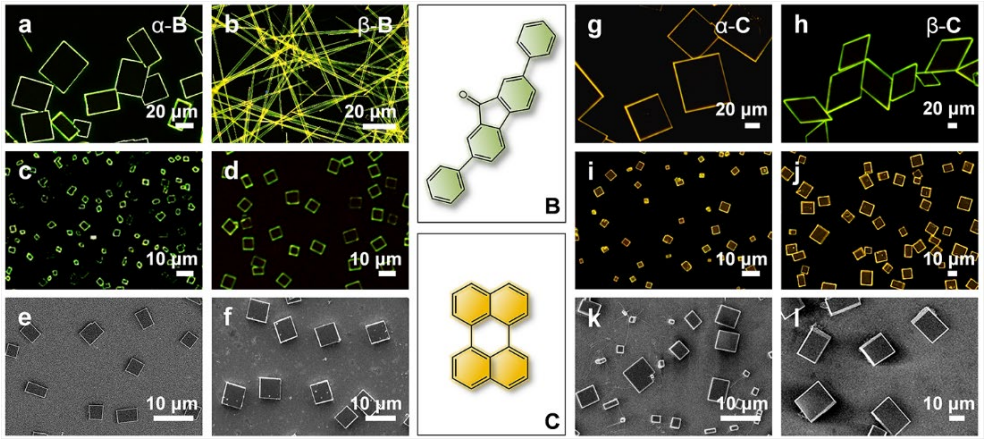


**Figure 5.** (a, b, g, h) FM images of (a) α-**B** and (b) β-**B** microcrystals as well as (g) α-**C** and (h) β-**C** microcrystals. (c, d, i, j) FM and (e, f, k, l) SEM images of the vapor-grown (c, e) α-**B** and (i, k)

α-**C** seeds as well as seed-induced (d, f) α-$\mathbf{B}_{\mathbf{second}}$ and (j, l) α-$\mathbf{C}_{\mathbf{second}}$ microcrystals. The middle region shows chemical structures of **B** and **C**. All samples were excited by UV light.

Note that pathway control for α- and β-form microcrystals of **B** or **C** has been realized, which inspire us to synthesize low-dispersity 2D microcrystals by the above seeding strategy. Taking **B** as an example, we further performed such a conceptual design by addition of a monomer solution of β-**B** MWs in DCM/ethanol (v/v = 1:1, $C_{\mathbf{B}}$ = 2.5 mM, $\mathbf{M}_{\mathbf{\beta\text{-}B}}$) onto the vapor-grown α-**B** MSs obtained at $H$ = 1500 μm and $T$ = 220 ℃ (Figure S22). Specifically, pure α-**B** MSs with a uniform thickness of 500 nm (Figures 5c,e and S23a) were used as seeds to induce the transformation of $\mathbf{M}_{\mathbf{\beta\text{-}B}}$. After evaporation of the mixture solvents, green-emitting 2D α-**B** MSs (α-$\mathbf{B}_{\mathbf{second}}$) of low dispersity and high crystallinity were readily obtained (Figures 5d,f and S24) and α-**B** seed MSs displayed additional thickness variation besides 2D homoepitaxial growth. Typically, single α-$\mathbf{B}_{\mathbf{second}}$ MS has a thickness of about 1.03–1.2 μm (Figure S23b), which has more than doubled. We speculated that the most stable (020) plane in α-**B** (the thickness plane) cannot easily be activated but the defective α-**B** seed MSs enable their reactivation on 3D crystal facets after addition of $\mathbf{M}_{\mathbf{\beta\text{-}B}}$ (Figures S23a, S25, and Table S7).

Not coincidentally, small-sized α-**C** MSs formed via microspacing PVT also function as seeds to yield low-dispersity α-$\mathbf{C}_{\mathbf{second}}$ MSs (Figures 5i,k,g,l, S26, and S27) by modulating the assembled pathway of a precursor solution of β-**C** MSs ($\mathbf{M}_{\mathbf{\beta\text{-}C}}$). Upon increasing the concentrations of the precursor solutions, α-**C** seed MSs with fewer defects and larger sizes were obtained, which initiate subsequent epitaxial growth mainly along the 2D direction instead of the thickness direction (Figure S26c,f,i,l). Contrarily, the mixtures of α- and β-**C** MSs were obtained by employing the solution-grown α-**C** MSs with larger dimension as seeds (Figure S28), further verifying living growth behavior of the vapor-grown seeds. Of particular interest were alloyed assemblies

composed of **C** and DCA that incorporate a small amount of DCA into the crystal lattices of α-**C** (**C**$_{1-x}$DCA$_x$, $x$ is the molar ratio of DCA).[50] Such a type of well-known alloys shows red emission as a consequence of energy transfer (ET) from α-**C** to **C**-DCA CT complex. We envisaged we can unveil the detailed processes of seed-induced pathway transformation by real-time recording epitaxial growth of red-emitting **C**$_{1-x}$DCA$_x$ on the orange-emitting α-**C** seed MSs.

Prior to this, we synthesized **C**$_{1-x}$DCA$_x$ assemblies ($x$ = 0.5%) following the solution synthetic conditions of pure α- and β-**C** MSs. Surprisingly, square α-**C**$_{1-x}$DCA$_x$ MSs instead of rhombic β-**C**$_{1-x}$DCA$_x$ MSs present uniform red emission (Figure S29a,b), possibly because different transition dipole orientations of **C** and **C**-DCA in the α- and β-**C** hosts leads to different ET efficiencies.[29] We again examined seed-induced pathway transformation by addition of a precursor solution of β-**C**$_{1-x}$DCA$_x$ MSs ($x$ = 0.5%, **M**$_{\beta\text{-}C}$′) onto the small-sized α-**C** seed MSs. As expected, thick square MSs with uniform red emission, low dispersity, and high crystallinity (α-**C**$_{second}$′) were obtained (Figures S29–S31). Meanwhile, we also recorded the real-time transformation processes under UV excitation (Figure S32 and Video 1). Within a short interval after addition of **M**$_{\beta\text{-}C}$′ solution ($t$ = 1 s), a low proportion of α-**C** seed MSs displays red emission at the sides. This implies that the **M**$_{\beta\text{-}C}$′ solution has reached supersaturation as the solvents evaporated, and free **C** and DCA molecules were co-deposited on the sides of the surviving α-**C** seed MSs. Afterwards ($t$ = 2, 6, and 7 s), more percentage of α-**C** seed MSs followed similar growth behavior, accompanied by the dimension increase. The central α-**C** MSs were always well recognized, verifying the self-seeding protocol. At $t$ = 14 and 21 s, the overwhelming majority of α-**C** seeds allowed an access to further monomer growth, and **M**$_{\beta\text{-}C}$′ transformed into red-emitting α-**C**$_{1-x}$DCA$_x$ alloys. Note that the α-**C** seed MSs exhibited a more significant increase in thickness compared to their sides. The real-time pathway

transformation processes offer us deeper insights into the formation mechanism of low-dispersity organic microcrystals.

In summary, we have realized polymorphism-controlled DSB-derived microcrystals of low dispersity by a seed-induced strategy. The thermodynamically and kinetically stable microcrystals were first obtained by the subtle control of pathway complexity. The small-sized α-form assemblies obtained by microspacing PVT can act as seeds to allow a good access to the further monomer growth. Consequently, the potentially occurring β-form microcrystals were inhibited and new added monomer exclusively assembled into α-form species, analogous to living supramolecular polymerization. After pathway transformation, the resulting α-form microcrystals present controlled lengths and area and high crystallinity. Polymorphism exists widely in π-conjugated molecular systems and such a seed-induced strategy for pathway control has demonstrated its efficacy in synthesizing polymorphic microcrystals of π-conjugated molecules with narrow size distributions, which may open the way for the construction of high-efficiency polymorphic micro- and nanoscale optoelectronic devices.

ASSOCIATED CONTENT

**Supporting Information**

The Supporting Information is available free of charge. Synthetic procedures and sample characterization, crystallographic data of α- and β-**A**, AFM profiles, additional SEM and FM images, PXRD patterns, PL and diffuse reflectance absorption spectra, summarized photophysical parameters, bright-field OM and POM images, predicted growth morphologies and molecular packing motifs

AUTHOR INFORMATION

**Corresponding Author**

*Email: wai-yeung.wong@polyu.edu.hk

*Email: iamzgmeng@njtech.edu.cn

*Email: yilonglei@tju.edu.cn.

**Author Contributions**

The manuscript was written through contributions of all authors. All authors have given approval to the final version of the manuscript. #These authors contributed equally.

**Notes**

The authors declare no competing financial interest.

ACKNOWLEDGMENT

The present work was dedicated in memory of Prof. Ian Manners for his remarkable contribution to the development of living self-assembly of BCPs. This work was supported by the National Natural Science Foundation of China (Grant Nos. 22090022, 21971189, 22075184, 22271153, and 52073242). Z.F. thanks to the Award Plan for Outstanding Innovation in Arts and Sciences from Tianjin University (B2-2022-003). W.-Y.W. also acknowledges the support from the Hong Kong Research Grants Council (Grant PolyU 153058/19P), the RGC Senior Research Fellowship Scheme (Grant SRFS2021-5S01), the CAS-Croucher Funding Scheme for Joint Laboratories (ZH4A), Miss Clarea Au for the Endowed Professorship in Energy (847S) and Research Institute for Smart Energy (CDAQ).

**Accession Codes**

CCDC 2321245 (for α-**A**) and 2321171 (for β-**A**) contain the supplementary crystallographic data for this paper. These data can be obtained free of charge via www.ccdc.cam.ac.uk/data_request/cif, or by emailing data_request@ccdc.cam.ac.uk, or by contacting The Cambridge Crystallographic Data Centre, 12 Union Road, Cambridge CB2 1EZ, UK; fax: +44 1223 336033.

REFERENCES


(1) Szwarc, M. 'Living' polymers. *Nature* **1956**, *178*, 1168–1169.

(2) Patterson, G. Sixty years of living polymers. *Nature* **2016**, *536*, 276–277.

(3) Wang, X.; Guerin, G.; Wang, H.; Wang, Y.; Manners, I.; Winnik, M. A. Cylindrical block copolymer micelles and co-micelles of controlled length and architecture. *Science* **2007**, *317*, 644−647.

(4) Gädt, T.; Ieong, N. S.; Cambridge, G.; Winnik, M. A.; Manners, I. Complex and hierarchical micelle architectures from diblock copolymers using living, crystallization-driven polymerizations. *Nat. Mater*. **2009**, *8*, 144–150.

(5) MacFarlane, L.; Zhao, C.; Cai, J.; Qiu, H.; Manners, I. Emerging applications for living crystallization-driven self-assembly. *Chem. Sci*. **2021**, *12*, 4661−4682.

(6) He, F.; Gädt, T.; Manners, I.; Winnik, M. A. Fluorescent "barcode" multiblock co-micelles via the living self-assembly of di- and triblock copolymers with a crystalline core-forming metalloblock. *J. Am. Chem. Soc*. **2011**, *133*, 9095−9103.

(7) Qiu, H.; Hudson, Z. M.; Winnik, M. A.; Manners, I. Multidimensional hierarchical self-assembly of amphiphilic cylindrical block comicelles. *Science* **2015**, *347*, 1329−1332.

(8) Han, L.; Wang, M.; Jia, X.; Chen, W.; Qian, H.; He, F. Uniform two-dimensional square assemblies from conjugated block copolymers driven by π–π interactions with controllable sizes. *Nat. Commun*. **2018**, *9*, 865.

(9) Shin, S.; Menk, F.; Kim, Y.; Lim, J.; Char, K.; Zentel, R.; Choi, T.-L. Living light-induced crystallization-driven self-assembly for rapid preparation of semiconducting nanofibers. *J. Am. Chem. Soc*. **2018**, *140*, 6088−6094.

(10) Lu, Y.; Lin, J.; Wang, L.; Zhang, L.; Cai, C. Self-assembly of copolymer micelles: higher-level assembly for constructing hierarchical structure. *Chem. Rev*. **2020**, *120*, 4111−4140.

(11) Wang, C.; Xu, L.; Zhou, L.; Liu, N.; Wu, Z.-Q. Asymmetric living supramolecular polymerization: Precise fabrication of one-handed helical supramolecular polymers. *Angew. Chem., Int. Ed*. **2022**, *61*, e202207028.

(12) Wan, Q.; To, W.-P.; Chang, X.; Che, C.-M. Controlled synthesis of $Pd^{II}$ and $Pt^{II}$ supramolecular copolymer with sequential multiblock and amplified phosphorescence. *Chem* **2020**, *6*, 945−967.

(13) Wan, Q.; To, W.-P.; Yang, C.; Che, C.-M. The metal-metal-to-ligand charge transfer excited state and supramolecular polymerization of luminescent pincer $Pd^{II}$-isocyanide complexes. *Angew. Chem., Int. Ed*. **2018**, *57*, 3089−3093.

(14) Zhang, W.; Jin, W.; Fukushima, T.; Saeki, A.; Seki, S.; Aida, T. Supramolecular linear heterojunction composed of graphite-like semiconducting nanotubular segments. *Science* **2011**, *334*, 340−343.

(15) Sarkar, A.; Behera, T.; Sasmal, R.; Capelli, R.; Empereur-Mot, C.; Mahato, J.; Agasti, S. S.; Pavan, G. M.; Chowdhury, A.; George, S. J. Cooperative supramolecular block copolymerization for the synthesis of functional axial organic heterostructures. J. *Am. Chem. Soc*. **2020**, *142*, 11528−11539.

(16) Ma, X.; Zhang, Y.; Zhang, Y.; Liu, Y.; Che, Y.; Zhao, J. Fabrication of chiral-selective nanotubular heterojunctions through living supramolecular polymerization. *Angew. Chem., Int. Ed*. **2016**, *55*, 9539−9543.

(17) Zhang, K.; Yeung, M. C.-L.; Leung, S. Y.-L.; Yam, V. W.-W. Living supramolecular polymerization achieved by collaborative assembly of platinum(II) complexes and block copolymers. *Proc. Natl. Acad. Sci. U.S.A*. **2017**, *114*, 11844−11849.

(18) Ogi, S.; Sugiyasu, K.; Manna, S.; Samitsu, S.; Takeuchi, M. Living supramolecular polymerization realized through a biomimetic approach. *Nat. Chem*. **2014**, *6*, 188−195.

(19) Sasaki, N.; Kikkawa, J.; Ishii, Y.; Uchihashi, T.; Imamura, H.; Takeuchi, M.; Sugiyasu, K. Multistep, site-selective noncovalent synthesis of two-dimensional block supramolecular polymers. *Nat. Chem*. **2023**, *15*, 922−929.

(20) Wagner, W.; Wehner, M.; Stepanenko, V.; Würthner, F. Supramolecular block copolymers by seeded living polymerization of perylene bisimides. *J. Am. Chem. Soc*. **2019**, *141*, 12044−12054.

(21) Wagner, W.; Wehner, M.; Stepanenko, V.; Ogi, S.; Würthner, F. Living supramolecular polymerization of a perylene bisimide dye into fluorescent J-aggregates. *Angew. Chem., Int. Ed.* **2017**, *56*, 16008−16012.

(22) Wehner, M.; Würthner, F. Supramolecular polymerization through kinetic pathway control and living chain growth. *Nat. Rev. Chem*. **2020**, *4*, 38−53.

(23) Matern, J; Dorca, Y.; Sánchez, L.; Fernández, G. Revising complex supramolecular polymerization under kinetic and thermodynamic control. *Angew. Chem., Int. Ed*. **2019**, *58*, 16730–16740.

(24) Wehner, M.; Röhr, M. I. S.; Bühler, M.; Stepanenko, V.; Wagner, W.; Würthner, F. Supramolecular polymorphism in one-dimensional self-assembly by kinetic pathway control. *J. Am. Chem. Soc.* **2019**, *141*, 6092–6107.

(25) Khanra, P.; Singh, A. K.; Roy, L.; Das, A. Pathway complexity in supramolecular copolymerization and blocky star copolymers by a hetero-seeding effect. *J. Am. Chem. Soc.* **2023**, *145*, 5270–5284.

(26) Datta, S.; Chaudhuri, D. Reversible supramolecular polymorphism in solution and solid matrix by manipulating sidegroup conformation. *Angew. Chem., Int. Ed*. **2022**, *61*, e202201956.

(27) Wang, K.; Zhang, H.; Chen, S.; Yang, G.; Zhang, J.; Tian, W.; Su, Z.; Wang, Y. Organic polymorphs: One-compound-based crystals with molecular-conformation- and packing-dependent luminescent properties. *Adv. Mater*. **2014**, *26*, 6168−6173.

(28) Gu, X.; Yao, J. J.; Zhang, G.; Yan, Y.; Zhang, C.; Peng, Q.; Liao, Q.; Wu, Y.; Xu, Z.; Zhao, Y.; Fu, H.; Zhang, D. Polymorphism-dependent emission for di(*p*-methoxylphenyl)dibenzofulvene and analogues: Optical waveguide/amplified spontaneous emission behaviors. *Adv. Funct. Mater*. **2012**, *22*, 4862−4872.

(29) Zhao, P.; Zhang, L.; Meng, Z.; Lei, Y. Multicomponent molecular assembly of fluorescent organic semiconductors beyond three compounds. *Adv. Funct. Mater*. **2022**, *32*, 2205092.

(30) Wang, K.; Xie, Y.; Liu, M.; Tao, W.; Zhang, H.; Huang, M.; You, J.; Liu, Y.; Li, Y.; Li, Z.; Dong, Y. Q. High-contrast polymorphic luminogen formed through effect of tiny differences in intermolecular interactions on the intramolecular charge transfer process. *Adv. Opt. Mater*. **2020**, *8*, 2000436.

(31) Ma, S.; Liu, Y.; Zhang, J.; Xu, B.; Tian, W. Polymorphism-dependent enhanced emission in molecular aggregates: J-aggregate versus X-aggregate. *J. Phys. Chem. Lett.* **2020**, *11*, 10504–10510.

(32) Ohtani, S.; Takeda, Y.; Gon, M.; Tanaka, K.; Chujo, Y. Facile strategy for obtaining luminescent polymorphs based on the chirality of a boron-fused azomethine complex. *Chem. Commun*. **2020**, *56*, 15305–15308.

(33) Echeverri, M.; Ruiz, C.; Gámez-Valenzuela, S.; Martín, I.; Carmen Ruiz Delgado, M.; Gutiérrez-Puebla, E.; Ángeles Monge, M.; Aguirre-Díaz, L. M.; Gómez-Lor, B. Untangling the mechanochromic properties of benzothiadiazole-based luminescent polymorphs through supramolecular organic framework topology. *J. Am. Chem. Soc*. **2020**, *142*, 17147–17155.

(34) Tang, B.; Liu, B.; Liu, H.; Zhang, H. Naturally and elastically bent organic polymorphs for multifunctional optical applications. *Adv. Funct. Mater*. **2020**, *30*, 2004116.

(35) Ghosh, T.; Birudula, S.; Kalita, K. J.; Vijayaraghavan, R. K. Control over kinetic and thermodynamically driven pathways of crystallization to yield cofacial and slipped-stack dimers in single crystals. *Chem. Eur. J.* **2020**, *26*, 10501−10509.

(36) Shi, J.; Yoon, S.-J.; Viani, L.; Park, S. Y.; Milián-Medina, B.; Gierschner, J. Twist-elasticity-controlled crystal emission in highly luminescent polymorphs of cyano-substituted distyrylbenzene (βDCS). *Adv. Opt. Mater*. **2017**, *5*, 1700340.

(37) Chen, P. Z.; Zhang, H.; Niu, L. Y.; Zhang, Y.; Chen, Y. Z.; Fu, H. B.; Yang, Q. Z. A solid-state fluorescent material based on carbazole-containing difluoroboron β-diketonate: Multiple chromisms, the self-assembly behavior, and optical waveguides. *Adv. Funct. Mater*. **2017**, *27*, 1700332.

(38) Zhang, X.; Gong, J.; Tao, W.; Jiang, X.; Chen, C.; Wei, P. Less is more: Tunable polymorphs with packing-dependent deep-red to near-infrared emission based on a geometrically simple molecule. *ACS Materials Lett*. **2022**, *4*, 1468–1474.

(39) Wang, X.; Qi, C.; Fu, Z.; Zhang, H.; Wang, J.; Feng, H.-T.; Wang, K.; Zou, B.; Lam, J. W. Y.; Tang, B. Z. A synergy between the push–pull electronic effect and twisted conformation for high-contrast mechanochromic AIEgens. *Mater. Horiz*. **2021**, *8*, 630–638.

(40) He, P.; Tu, Z.; Zhao, G.; Zhen, Y.; Geng, H.; Yi, Y.; Wang, Z.; Zhang, H.; Xu, C.; Liu, J.; Lu, X.; Fu, X.; Zhao, Q.; Zhang, X.; Ji, D.; Jiang, L.; Dong, H.; Hu, W. Tuning the crystal polymorphs of alkyl thienoacene via solution self-assembly toward air-stable and high-performance organic field-effect transistors. *Adv. Mater*. **2015**, *27*, 825–830.

(41) Zhang, Z.; Jiang, L.; Cheng, C.; Zhen, Y.; Zhao, G.; Geng, H.; Yi, Y.; Li, L.; Dong, H.; Shuai, Z.; Hu, W. The impact of interlayer electronic coupling on charge transport in organic semiconductors: A case study on titanylphthalocyanine single crystals. *Angew. Chem., Int. Ed.* **2016**, *55*, 5206–5209.

(42) Potticary, J.; Terry, L. R.; Bell, C.; Papanikolopoulos, A. N.; Christianen, P. C. M.; Engelkamp, H.; Collins, A. M.; Fontanesi, C.; Kociok-Köhn, G.; Crampin, S.; Da Como, E.; Hall, S. R. An unforeseen polymorph of coronene by the application of magnetic fields during crystal growth. *Nat. Commun*. **2016**, *7*, 11555.

(43) Zhou, Q.; Lei, Y.; Fu, H. A molecular design principle towards luminescent polymorphic organic heterostructured architectures. *J. Mater. Chem. C* **2021**, *9*, 489–496.

(44) Han, X.; Lei, Y.; Liao, Q.; Fu, H. Color- and dimension-tunable light-harvesting organic charge-transfer alloys for controllable photon-transport photonics. *Angew. Chem., Int. Ed*. **2021**, *60*, 3037–3046.

(45) Qian, J.; Lu, Y.; Chia, A.; Zhang, M.; Rupar, P. A.; Gunari, N.; Walker, G. C.; Cambridge, G.; He, F.; Guerin, G.; Manners, I.; Winnik, M. A. Self-seeding in one dimension: A route to uniform fiber-like nanostructures from block copolymers with a crystallizable core-forming block. *ACS Nano* **2013**, *7*, 3754–3766.

(46) Xu, J.; Ma, Y.; Hu, W.; Rehahn, M.; Reiter, G. Cloning polymer single crystals through self-seeding. *Nat. Mater*. **2009**, *8*, 348–353.

(47) Wang, Z.; Ma, C.; Huang, X.; Lu, G.; Winnik, M. A.; Feng, C. Self-seeding of oligo(*p*-phenylenevinylene)-*b*-poly(2-vinylpyridine) micelles: Effect of metal ions. *Macromolecules* **2021**, *54*, 6705–6717.

(48) Ye, X.; Liu, Y.; Han, Q.; Ge, C.; Cui, S.; Zhang, L.; Zheng, X.; Liu, G.; Liu, J.; Liu, D.; Tao, X. Microspacing in-air sublimation growth of organic crystals. *Chem. Mater*. **2018**, *30*, 412−420.

(49) He, T.; Stolte, M.; Burschka, C.; Hansen, N. H.; Musiol, T.; Kalblein, D.; Pflaum, J.; Tao, X.; Brill, J.; Würthner, F. Single-crystal field-effect transistors of new $Cl_2$-NDI polymorph processed by sublimation in air. *Nat. Commun*. **2015**, *6*, 5954.

(50) Hai, T.; Feng, Z.; Sun, Y.; Wong, W.-Y.; Liang, Y.; Zhang, Q.; Lei, Y. Vapor-phase living assembly of π-conjugated organic semiconductors. *ACS Nano* **2022**, *16*, 3290–3299.

(51) Varghese, S.; Yoon, S.-J.; Calzado, E. M.; Casado, S.; Boj, P. G.; Diaz-Garcia, M. A.; Resel, R.; Fischer, R.; Milian-Medina, B.; Wannemacher, R.; Park, S. Y.; Gierschner, J. Stimulated resonance Raman scattering and laser oscillation in highly emissive distyrylbenzene-based molecular crystals. *Adv. Mater.* **2012**, *24*, 6473–6478.

(52) Gierschner, J.; Varghese, S.; Park, S. Y. Organic single crystal lasers: A materials view. *Adv. Opt. Mater*. **2016**, *4*, 348–364.

(53) Feng, Z.; Hai, T.; Zhang, L.; Lei, Y. Fractal branched microwires of organic semiconductor with controlled branching and low-threshold amplified spontaneous emission. *Nano Lett*. **2023**, *23*, 835–842.

(54) Zhang, C.; Yan, Y.; Zhao, Y. S.; Yao, J. From molecular design and materials construction to organic nanophotonic devices. *Acc. Chem. Res*. **2014**, *47*, 3448–3458.

(55) Korevaar, P. A.; George, S. J.; Markvoort, A. J.; Smulders, M. M. J.; Hilbers, P. A. J.; Schenning, A. P. H. J.; De Greef, T. F. A.; Meijer, E. W. Pathway complexity in supramolecular polymerization. *Nature* **2012**, *481*, 492–496.

(56) Wang, F.; Liao, R.; Wang, F. Pathway control of π-conjugated supramolecular polymers by incorporating donor-acceptor functionality. *Angew. Chem., Int. Ed*. **2023**, *62*, e202305827.

(57) Xu, J.; Semin, S.; Niedzialek, D.; Kouwer, P. H. J.; Fron, E.; Coutino, E.; Savoini, M.; Li, Y.; Hofkens, J.; Uji-I, H.; Beljonne, D.; Rasing, T.; Rowan, A. E. Self-assembled organic microfibers for nonlinear optics. *Adv. Mater*. **2013**, *25*, 2084−2089.

(58) Xu, J.; Semin, S.; Cremers, J.; Wang, L.; Savoini, M.; Fron, E.; Coutino, E.; Chervy, T.; Wang, C.; Li, Y.; Liu, H.; Li, Y.; Tinnemans, P.; Kouwer, P. H.; Ebbesen, T. W.; Hofkens, J.; Beljonne, D.; Rowan A. E.; Rasing, T. Controlling microsized polymorphic architectures with distinct linear and nonlinear optical properties. *Adv. Opt. Mater*. **2015**, *3*, 948−956.

(59) Pick, A.; Klues, M.; Rinn, A.; Harms, K.; Chatterjee, S.; Witte, G. Polymorph-selective preparation and structural characterization of perylene single crystals. *Cryst. Growth Des*. **2015**, *15*, 5495–5504.